

Shape from Projections via Differentiable Forward Projector

Jakeoung Koo¹, Qiongyang Chen², J. Andreas Brentzen¹, Anders B. Dahl¹,
and Vedrana A. Dahl¹

¹ Technical University of Denmark, Kgs. Lyngby, Denmark
{jakoo, janba, abda, vand}@dtu.dk

² University of Antwerp, Antwerp, Belgium
qiongyang.chen@uantwerpen.be

Abstract. In tomography, forward projection of 3D meshes has been mostly studied to simulate data acquisition. However, such works did not consider an inverse process of estimating shapes from projections. In this paper, we propose a differentiable forward projector for 3D meshes, to bridge the gap between the forward model for 3D surfaces and optimization. We view the forward projection as a rendering process, and make it differentiable by extending a recent work in differentiable rasterization. We use the proposed forward projector to reconstruct 3D shapes directly from projections. Experimental results for single-object problems show that our method outperforms the traditional voxel-based methods on noisy simulated data. We also apply our method on real data from electron tomography to estimate the shapes of some nanoparticles.

1 Introduction

In computed tomography (CT), we aim at solving the inverse problem of computing the 3D structure (shape and attenuation) of an object from a set of projection images [1] taken from different angles. Here, the geometry and the physics of the imaging system is known, which allows us to model the forward process, i.e. if we have a suggestion for the 3D structure of the imaged object, we can compute the projection images.

We need a data structure to represent the structure of the object that should be reconstructed. The most common data structure is a volumetric image, with voxel intensities representing local attenuation. This approach may be used for reconstructing any type of object. However, in situations with projections from a limited angular view or noisy data, it can be difficult to accurately compute the attenuations in all voxels. Therefore, we propose to use a mesh to represent the shape of the object. The mesh separates the object into parts with a constant attenuation.

In tomography, forward projection of 3D meshes has mostly been used for simulating tomographic data acquisition, i.e. modeling the forward projection. This includes modeling X-ray transmission imaging based on Monte-Carlo methods [2,3] or ray tracing techniques [3,4]. Furthermore, Vidal et al. [5,6] took the

advantage of the OpenGL library to simulate X-ray images in real time. However, none of the proposed methods are concerned with reconstruction, i.e. solving the inverse problem.

For the mesh-based tomographic reconstruction that we propose, the reconstruction problem is two-fold. The mesh must be deformed to follow the boundaries of the depicted object, and in each part of the object, a single attenuation coefficient must be estimated. We employ rendering techniques, which allows a very efficient projection of the 3D mesh to the detector plane. Similar to [5] we extend the differentiable rasterizer recently proposed in [7] to derive a differentiable forward projection. This enables us to compute vertex displacements that deform the mesh based on the difference between the forward projection and the measured projection images.

Our model can be used for any modality where the penetrating rays give pixel intensities which are linear combinations of the ray path lengths in different materials, each material contributing with a coefficient. This is valid for X-ray CT where we deal with X-ray attenuation coefficient [1], and is assumed in electron tomography [8] where coefficient is related to electron scattering [9].

In summary, our contribution is two-fold. We suggest a differentiable forward projector to generate projections from 3D meshes, and we propose a shape estimation method employing the differentiable forward projector. Our code will be made available online.

2 Related works

Our approach requires deforming the mesh using differentiable rasterization, and here we describe the methods related to our work.

Differentiable rasterizer. To use the rendering process for inference, several works have proposed methods for making rasterization rendering differentiable. The general framework OpenDR, that was proposed by Loper and Black [10], approximates gradients of pixel values with respect to model parameters. Several works are related to deep learning, where rendering process has been made differentiable to be incorporated into neural networks. Kato et al., [11] suggested a heuristic forward and backward pass where blurring is used to avoid zero gradients. This approach has an inconsistency between the forward and backward pass, and to circumvent this inconsistency, [12] proposed a method called SoftRas by relaxing discrete rasterization process into the aggregation of smooth probability functions. Unlike the common rasterization rendering, in SoftRas, each face in the mesh affects many pixels in the image plane, which is computationally costly and memory-demanding.

Chen et al. [7] suggested an interpolation-based differentiable rasterizer called DIB-R. It reformulates the barycentric interpolation in the rasterization process to analytically derive the gradients. Our forward projector uses this reformulation when computing the thickness of an object, but differs in some aspects. DIB-R can improve the performance by ignoring invisible faces for background

pixels, but since we model penetrating radiation, our forward projector needs to consider all the faces. DIB-R uses the idea of SoftRas [12] for background pixels to propagate the gradients on those background, but our forward projector does not use it to reduce the computational cost.

Shape reconstruction from projections. Our proposed method is related to tomographic segmentation, where segments are directly computed from projections. This includes [13,14,15] that are based on the Mumford-Shah model [16] where boundaries are represented using level-sets [17]. Recently, the parametric level-set method [18] has been used for tomographic segmentation in [19,20] where level-sets are represented as an aggregation of radial basis functions. Although the parametric level-set method has fewer unknown variables, its forward projection still depends on a regular grid. On the other hand, the work [21] based on snakes [22] avoids a voxel grid – it represents curves explicitly and proposes a direct forward projection of the curves. However, this method is limited to a single 2D curve, while our method supports 3D objects. Another difference is that [21] evolves curves in the normal directions of curve points, while our deformation can displace the vertices in all directions.

3 Differentiable forward projector

In this section, we describe our main contribution of the differentiable forward projector. The goal is to forward project triangular meshes and make this process differentiable with respect to 3D vertex positions and attenuation coefficients. This differentiable forward projection will be used for optimizing the mesh shape described in Sec. 4. First we describe the case of a single object and then extend to composite objects.

3.1 Single object

Consider an object represented by a watertight triangle mesh. The object is homogeneous, i.e. it has a certain attenuation coefficient μ associated with the volume inside the mesh. For now, we consider μ constant, but its derivative will be explained later. The mesh consists of K vertices, and we write \mathbf{v}_k for the 3D coordinates of the vertex k .

We now sketch the forward projection of the object onto the detector for one projection angle. However, in general, we have multiple detector positions and orientations. Let \mathbf{P} and \mathbf{R} be the position of the detector and a matrix that rotates from detector coordinates to the global frame, respectively. If we denote the position of vertex k in global coordinates by \mathbf{V}_k , the position in detector coordinates are $\mathbf{v}_k = \mathbf{R}^\top(\mathbf{V}_k - \mathbf{P})$. Note that in detector coordinates, the detector itself corresponds to the plane $z = 0$, its center is at the origin, and the positive z -axis points towards the object, see Fig. 1.

Expressed in detector coordinates, the distance of the vertex k from the detector is trivially $l_k = \mathbf{z}^\top \mathbf{v}_k$ while $\mathbf{s}_k = [\mathbf{x} \ \mathbf{y}]^\top \mathbf{v}_k$ are the coordinates of the

projection of the vertex onto the detector. Here \mathbf{x} , \mathbf{y} , and \mathbf{z} are unit vectors in x , y and z direction, for example $\mathbf{x} = [1\ 0\ 0]^\top$.

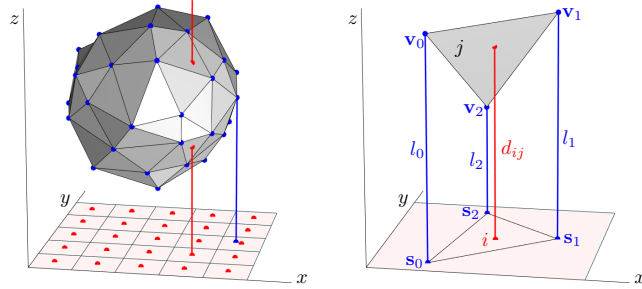


Fig. 1. *Left:* The vertices of the triangle mesh (blue dots) are projected onto the detector. Each detector pixel (red dots) is associated with the projection ray which intersects with the projection mesh triangles. *Right:* One triangle j , here given by vertices $k = 0, 1, 2$, and one detector pixel i . Using barycentric coordinates, the distance d_{ij} may be expressed in terms of l_k .

Projecting the object onto the detector pixel i we consider projection ray associated with i (slightly sloppy, call it ray i), and its path length in the object. As explained in [5], this can be broken into contribution of all intersections of the ray i with the mesh triangles

$$p_i = \mu \sum_{\substack{j \\ i \text{ intersects } j}} \text{sign}(\mathbf{z}^\top \mathbf{n}_j) d_{ij} \quad (1)$$

where \mathbf{n}_j is the normal of the triangle j (needed for determining the sign of the contribution), and d_{ij} is the distance of the intersection point to the detector.

Considering now a single triangle j we express d_{ij} using barycentric coordinates

$$d_{ij} = \sum_{\substack{k \\ k \text{ in } j}} w_{ij}^k l_k, \quad (2)$$

where k are the indices of the three vertices of the triangle j and w_{ij}^k are the corresponding three barycentric coordinates of pixel i with respect to the projection of triangle j onto the detector plane, see Fig. 1, *right*.

To make the forward projection differentiable, we derive

$$\frac{\partial p_i}{\partial \mathbf{v}_k} = \mu \sum_{\substack{j \\ i \text{ intersects } j}} \text{sign}(\mathbf{z}^\top \mathbf{n}_j) \frac{\partial d_{ij}}{\partial \mathbf{v}_k}, \quad (3)$$

and

$$\frac{\partial d_{ij}}{\partial \mathbf{v}_k} = \sum_{\substack{k \\ k \text{ in } j}} \left(w_{ij}^k \frac{\partial l_k}{\partial \mathbf{v}_k} + \frac{\partial w_{ij}^k}{\partial \mathbf{v}_k} l_k \right) = \sum_{\substack{k \\ k \text{ in } j}} \left([0 \ 0 \ w_{ij}^k] + \frac{\partial w_{ij}^k}{\partial \mathbf{v}_k} l_k \right). \quad (4)$$

For the last step, computation of $\partial w_{ij}^k / \partial \mathbf{v}_k$, we employ the idea from [7], which reformulates the barycentric form to express the coefficients w_{ij}^k in terms of 2D projected positions \mathbf{s}_k and the position of detector pixel i .

3.2 Composite objects

The method described above generalizes to composite objects if certain conditions are met. Specifically, we require that we know beforehand the topology of the parts of the composites, and how parts are embedded within one another. Thus, for each interface triangle we will know what class of material is on either side, but we do not know the specific attenuation coefficient of the classes, since we solve for those.

In order to extend Eq. (1) to composites, we only have to observe that triangles may now be the interface between two materials and not just air and material. This can be handled simply by letting each triangle contribute twice:

$$p_i = \sum_j \mu_j \text{sign}(\mathbf{z}^\top \mathbf{n}_j) d_{ij} - \sum_j \bar{\mu}_j \text{sign}(\mathbf{z}^\top \mathbf{n}_j) d_{ij} \quad (5)$$

$$= \sum_j (\mu_j - \bar{\mu}_j) \text{sign}(\mathbf{z}^\top \mathbf{n}_j) d_{ij}, \quad (6)$$

where μ_j is the attenuation of the interior material and $\bar{\mu}_j$ of the exterior material according to normal orientation. Of course, either attenuation will be zero if the material on the corresponding side of the triangle is air.

The derivative of a pixel value with respect to attenuation coefficient μ_m for material m (by abuse of notation) is

$$\frac{\partial p_i}{\partial \mu_m} = \sum_j \pm \text{sign}(\mathbf{z}^\top \mathbf{n}_j) d_{ij}, \quad (7)$$

where the \pm is positive if the interior material of face j is labeled as m and negative if m is the exterior material. We also modify Eq. (3) by changing μ to $(\mu_j - \bar{\mu}_j)$.

We have derived the Jacobians in Eq. (3) and (7), which will be used to optimize an objective function E . That is, we can propagate the gradients from E :

$$\frac{\partial E}{\partial \mathbf{v}_k} = \sum_i \frac{\partial E}{\partial p_i} \frac{\partial p_i}{\partial \mathbf{v}_k}, \quad \frac{\partial E}{\partial \mu_m} = \sum_i \frac{\partial E}{\partial p_i} \frac{\partial p_i}{\partial \mu_m}, \quad (8)$$

where the summation is over all the detector pixels.

4 Shape from projections

In this section, we use the proposed forward projector to reconstruct shapes from projections. We assume that a template mesh with the correct topology is given. We aim to deform the template mesh and estimate the attenuation coefficients by minimizing the residual between data \hat{p} and our estimation p .

Optimizing only the data fitting term can lead to degenerate meshes. To obtain high-quality meshes, we impose three regularization terms. The first term is the Laplacian term [23], which constrains the vertices to move similarly with their neighbors, defined by $E_{\text{lap}} = \sum_k \|\mathbf{V}_k - \frac{1}{|\mathcal{N}(k)|} \sum_{n \in \mathcal{N}(k)} \mathbf{V}_n\|^2$, where $\mathcal{N}(k)$ is the index set of neighboring vertices to k -th vertex. The second term is the edge length term to penalize long edges: $E_{\text{edge}} = \sum_{(\mathbf{v}_k, \mathbf{v}_n) \in G} \|\mathbf{V}_k - \mathbf{V}_n\|^2$, where G denotes the set of edges. Lastly, we impose the flattening term [11]: $E_{\text{flat}} = \sum_{e \in G} (1 + \cos \theta_e)^2$, where θ_e denotes the angle between the normal vectors of two faces sharing the edge e . Flattening term is needed to remove near-zero volume spikes. These thin artifacts have negligible contribution to the forward projection, and will be ignored by the data fitting term. As shown in Fig. 2, such artifacts can appear during the deformation, but disappear later.

With the data fidelity and regularization terms, the objective function to minimize is:

$$E(\{\mathbf{V}_k\}, \{\mu_m\}) = \|p - \hat{p}\|_2^2 + \alpha E_{\text{lap}} + \beta E_{\text{edge}} + \gamma E_{\text{flat}} \quad (9)$$

where α, β, γ control the relative weights between the terms. Note that the size of projection data \hat{p} is the number of detector pixels times the number of projection angles. We use automatic differentiation to minimize E . For large projection data, we can use stochastic gradient descent with mini batches in terms of projection angles. In this paper, however, we only consider full batch size of data.

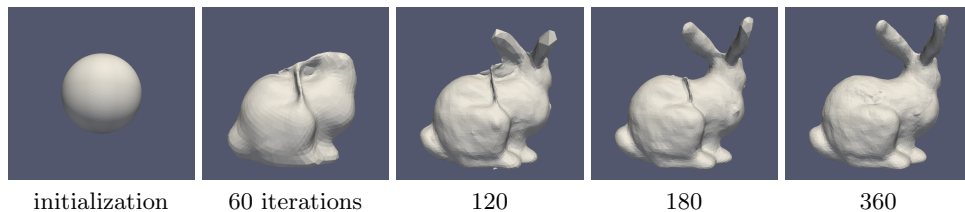


Fig. 2. Deformation example, where the mesh was refined at iteration 60, 120, 180.

5 Experimental results

In this section, we present the experimental results of our method on synthetic data of single objects. We also show the results on real data of a composite object from electron tomography, which has limited range of angles.

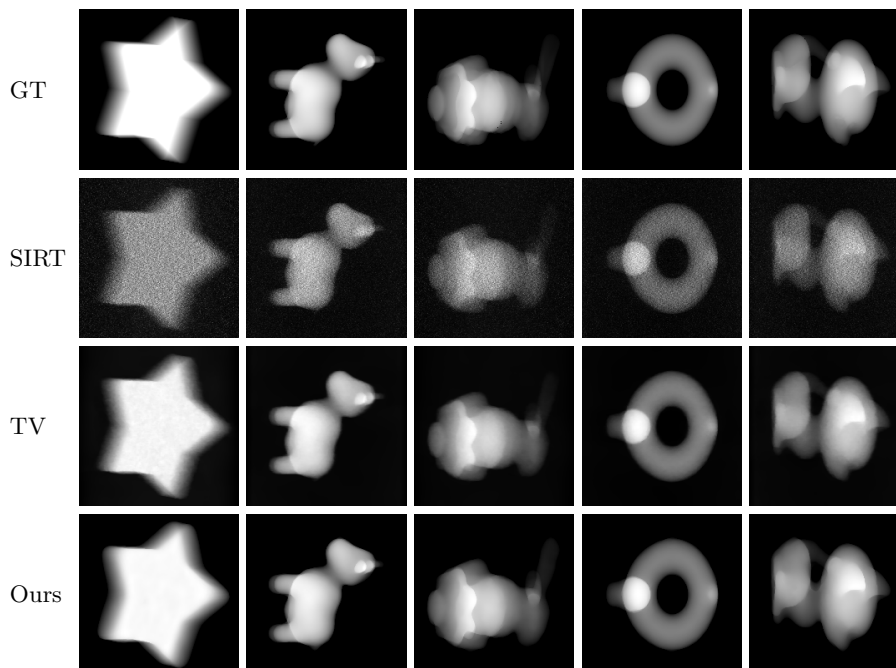


Fig. 3. Qualitative results of estimated projections on noisy data with relative noise level 0.4. The first row shows the ground truth, *i.e.*, noise-free data. 2nd-5th row show the estimated projections by SIRT, TV and the proposed method, respectively.

5.1 Shape reconstruction of watertight objects

Datasets. This experiment is designed to test our shape estimation method on noisy simulated data. We use 5 watertight meshes (star, spot [24], bunny, bob, kitten), shown in the first row of Fig. 4. The attenuation of the objects are set to 1. Generating projections of those meshes using our forward model may resemble to the so-called inverse crime [25]. To avoid it, we employ the Blender software [26] to make projection data based on ray casting methods similar to [4]. We use 3D parallel projection geometry with 30 projection angles and the detector of size 192×192 pixels. The data are shown in the first row of Fig. 3 for one projection view.

Evaluation metrics. We compare our result to two standard reconstruction methods: simultaneous iterative reconstruction technique (SIRT) [27] and total variation (TV) based reconstruction [28,29]. These methods yield 3D images, whereas our method produces surface mesh, making direct comparison of the main output challenging. For consistent comparison, we employ a residual-based metric: *residual projection error* [30], which measures the L^2 norm difference of data and estimated projections. We impose the relative Gaussian noise on

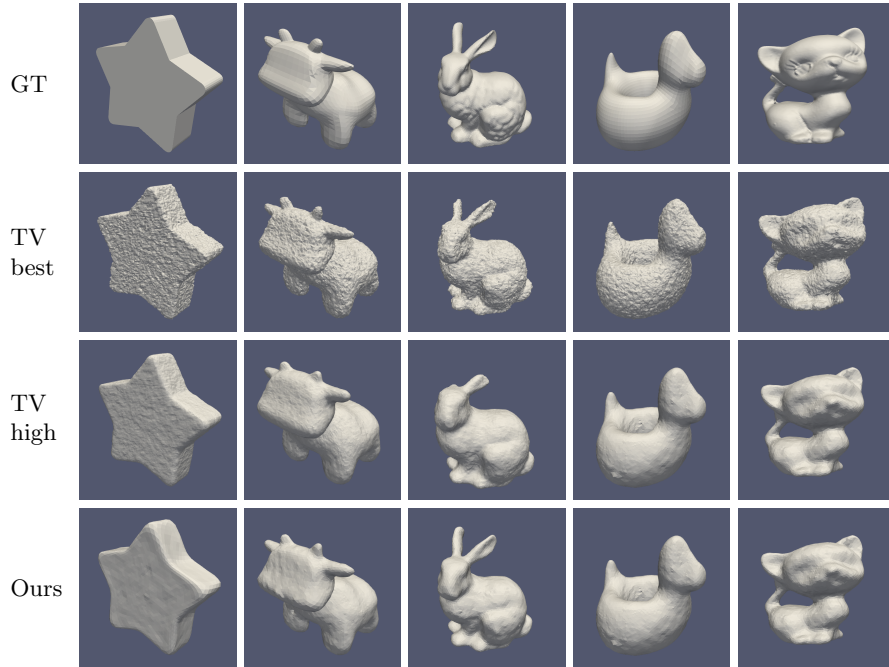


Fig. 4. Qualitative results of estimated meshes on noisy data with relative noise level 0.4. The top row shows the ground truth meshes. Rows 2 and 3 show the extracted isosurface from the results of TV reconstruction with the optimal regularization parameter (best) and a high regularization parameter (high), respectively. The last row shows our results.

the original data and calculate the residual projection error between noise-free projections and the estimations of other methods and our method. For SIRT and TV, the reconstruction voxel size is set as $192 \times 192 \times 192$ and the algorithm parameters are chosen carefully.

Implementation details. Our implementation relies on PyTorch [31] and uses Adam [32] as an optimizer with the parameters ($\beta_1 = 0.9$, $\beta_2 = 0.999$). The proposed forward projector is implemented as a layer in PyTorch. As for the regularization parameters, we fix $\alpha = 10$, $\gamma = 0.01$ and iterate 500 times. The step size τ (learning rate in PyTorch) is set to 0.01 and reduced by half at 400 iteration. During the experiment, we only vary the edge length parameter β . As for initialization, our method begins from an icosphere for genus-0 objects, and from a torus for genus-1 objects. Except for *star* data, we refine the mesh by [33] at iteration 60 and improve the mesh quality 3 times by a lightweight repair method [34] at iteration 60, 120, 180. These refine and repair steps help remove artifacts and lead to fast convergence.

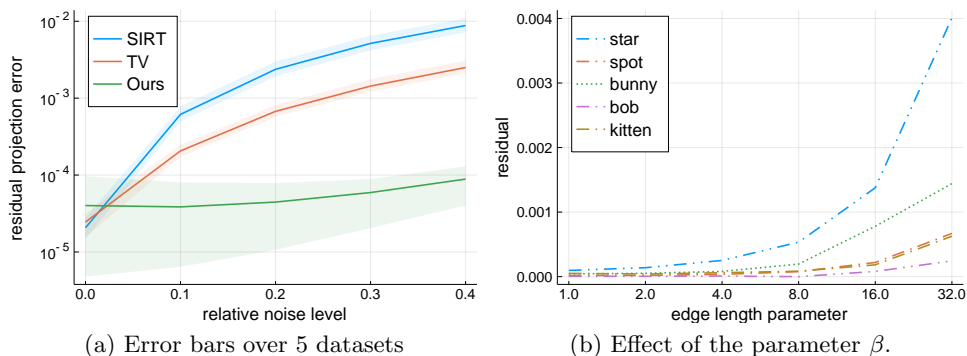


Fig. 5. Quantitative results. In (a), the error bars denote the average values with the maximum and minimum value; and the y-axis is in logarithmic scale. (b) shows the residual on noise-free data by our method.

Robustness to noise. Our experiments show that the proposed method is robust to noise. Fig. 3 shows reconstructions from noisy data with relative noise level 0.4 achieved using SIRT, TV reconstruction and our method. Since SIRT has no regularization it fits closely to the highly noisy data. The results of TV are relatively smooth, but sharp transitions appear blurred. On the other hand, the proposed method yields projections similar to noise-free data. Fig. 4 shows the final mesh results, where the proposed method yields qualitatively better results than TV – we omit highly noisy SIRT results. In Fig. 5 (a), we provide the quantitative results of residual projection error with respect to relative noise levels. Without noise, SIRT gives the superior result as it fits to data without regularization. However, as noise increases, the results of SIRT and TV are shown to be poorer. In (b), we show the effect of edge length parameter on noise-free data. The residual is large for *star* data, due to the coarse resolution of mesh. We observe that if the edge length parameter is less than 1.0, the final meshes might have some artifacts.

Computational cost. Table 1 shows the size of the initial and final mesh and running times. As we do not refine the mesh for *star* object, its computational cost is lower than others. We do the experiment on a Ubuntu server with 256GB RAM and Titan X GPU.

data	star	spot	bunny	bob	kitten
initial mesh	icosphere (1280 faces)			torus (3200 faces)	
final mesh (# of faces)	no refine.	18680	17908	19308	20904
running time (sec)	244.1	730.7	719.6	816.3	816.8

Table 1. Size of meshes and running times

5.2 Application to electron tomography

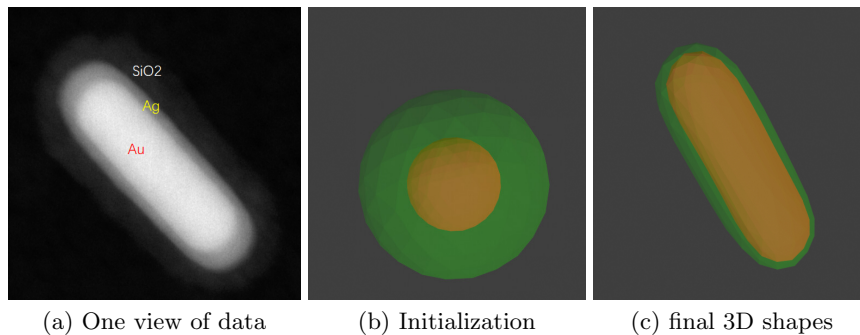


Fig. 6. Projection data and rendering of our results.

Datasets. The goal of this reconstruction is to estimate the shape of a composite object having Au-core and Ag-shell nanorods and to compute the relative atomic contents between them. We obtain the data with a similar setting to [35] except for the tilt ranges (projection angles). The data consist of 49 tilt angles between -72° to 72° and the detector of size 648×648 pixels. Fig. 6 (a) shows one projection view of the data, where silica is only used to fix the shapes during the acquisition.

Evaluation quantity. To compute the relative atomic contents from our final meshes, we first compute the volumes V_{Au} , V_{Ag} of two output meshes and estimate the number of atoms N_{Au} , N_{Ag} , respectively.³ Then, the relative atomic content for Au can be computed by $N_{\text{Au}}/(N_{\text{Au}} + N_{\text{Ag}})$. To validate the results, we compare our result to [36] which is based on Energy Dispersive X-ray Spectroscopy (EDXS) in a transmission electron microscopy. EDXS can obtain reliable quantitative chemical information of materials by using the characteristic X-rays [36]. We consider the result of EDXS as the reference to evaluate our results.

Implementation details. We run 200 iterations with $\alpha = 10$, $\beta = 0$, $\gamma = 0$ and initialize the shapes as two icospheres with 160 faces. To remove the unnecessary parts from SiO₂, we subtract the data by 0.1 times its maximum value and set negative values as zeros. We use the collision detection method in [37], to make sure that the two nanorodes do not collide. In this experiment, we set the step size $\tau = 0.005$ and observe no collisions.

Results. Fig. 6 (c) shows our final estimated 3D shapes from (b) the two icospheres. Table 2 provides the quantitative results of relative atomic contents.

³ $N_{\text{Au}} = A_{\text{Au}}V_{\text{Au}}/M_{\text{Au}}$ where A_{Au} is the bulk density of Au; V_{Au} its volume; and M_{Au} its relative atomic mass.

	EDXS [36]	Voxel-based [35]	Proposed
Au (%)	58.73	59.80	59.36
Ag (%)	41.27	40.20	40.64

Table 2. Estimated relative atomic contents.

The results of both ours and voxel-based method [35] are close to the reference result by EDXS. An advantage of our method is that our method directly solves shapes without a post-processing, whereas [35] needs a post processing of applying morphological operators, after image reconstruction.

6 Conclusion

Compared with other reconstruction methods, our approach has significant advantages when reconstructing homogeneous objects with relatively simple geometry, and when the data foundation is noisy or limited. Here, we explained our method in parallel geometry where rays are perpendicular to the detector plane, but it may be extend to a more general setting such as cone beam geometry [1].

References

1. Buzug, T.M.: Computed Tomography from Photon Statistics to Modern Cone Beam CT. Springer (2008)
2. Bonin, A., Chalmond, B., Lavayssière, B.: Monte-Carlo simulation of industrial radiography images and experimental designs. *NDT & E International* **35** (2002)
3. Freud, N., Duvauchelle, P., Létang, J.M., Babot, D.: Fast and robust ray casting algorithms for virtual X-ray imaging. *Nuclear Instruments and Methods in Physics Research Section B: Beam Interactions with Materials and Atoms* **248** (2006)
4. Marinovszki, Á., Beenhouwer, J.D., Sijbers, J.: An efficient CAD projector for X-ray projection based 3D inspection with the ASTRA Toolbox. In: *Conference on Industrial Computed Tomography*. (2018)
5. Vidal, F.P., Garnier, M., Freud, N., Létang, J.M., John, N.W.: Simulation of X-ray attenuation on the GPU. In: *Proceedings of Theory and Practice of Computer Graphics*, Cardiff, UK, Eurographics Association (2009)
6. Sujar, A., Meuleman, A., Villard, P.F., Garcia, M., Vidal, F.: gVirtualXRay: Virtual x-ray imaging library on GPU. In: *Computer Graphics and Visual Computing (CGVC)*. (2017)
7. Chen, W., Gao, J., Ling, H., Smith, E.J., Lehtinen, J., Jacobson, A., Fidler, S.: Learning to Predict 3D Objects with an Interpolation-based Differentiable Renderer. In: *Neural Information Processing Systems*. (2019)
8. Aveyard, R., Zhong, Z., Batenburg, K.J., Rieger, B.: Optimizing experimental parameters for the projection requirement in HAADF-STEM tomography. *Ultra-microscopy* **177** (2017)
9. Midgley, P.A., Dunin-Borkowski, R.E.: Electron tomography and holography in materials science. *Nature Materials* **8** (2009)
10. Loper, M.M., Black, M.J.: OpenDR: An Approximate Differentiable Renderer. In: *European Conference on Computer Vision*. (2014)

11. Kato, H., Ushiku, Y., Harada, T.: Neural 3D Mesh Renderer. In: IEEE Conference on Computer Vision and Pattern Recognition. (2018)
12. Liu, S., Chen, W., Li, T., Li, H.: Soft Rasterizer: Differentiable Rendering for Unsupervised Single-View Mesh Reconstruction. International Conference on Computer Vision (2019)
13. Elangovan, V., Whitaker, R.T.: From Sinograms to Surfaces: A Direct Approach to the Segmentation of Tomographic Data. In: Medical Image Computing and Computer-Assisted Intervention (MICCAI). (2001)
14. Whitaker, R.T., Elangovan, V.: A direct approach to estimating surfaces in tomographic data. *Medical Image Analysis* **6** (2002)
15. Alvino, C.V., Yezzi, A.J.: Tomographic reconstruction of piecewise smooth images. In: IEEE Conference on Computer Vision and Pattern Recognition. (2004)
16. Mumford, D., Shah, J.: Optimal approximations by piecewise smooth functions and associated variational problems. *Communications on pure and applied mathematics* **42** (1989)
17. Osher, S., Fedkiw, R.: Level set methods and dynamic implicit surfaces. *Applied Mechanics Reviews* **57** (2004)
18. Aghasi, A., Kilmer, M., Miller, E.L.: Parametric Level Set Methods for Inverse Problems. *SIAM Journal on Imaging Sciences* **4** (2011)
19. Kadu, A., van Leeuwen, T., Batenburg, K.J.: A parametric level-set method for partially discrete tomography. In: International Conference on Discrete Geometry for Computer Imagery. (2018)
20. Eliasof, M., Sharf, A., Treister, E.: Multi-modal 3D Shape Reconstruction Under Calibration Uncertainty using Parametric Level Set Methods. arXiv:1904.10379 [cs] (2019)
21. Dahl, V.A., Dahl, A.B., Hansen, P.C.: Computing segmentations directly from x-ray projection data via parametric deformable curves. *Measurement Science and Technology* **29** (2018)
22. Kass, M., Witkin, A., Terzopoulos, D.: Snakes: Active contour models. *International Journal of Computer Vision* **1** (1988)
23. Wang, N., Zhang, Y., Li, Z., Fu, Y., Liu, W., Jiang, Y.G.: Pixel2Mesh: Generating 3D Mesh Models from Single RGB Images. In: European Conference on Computer Vision. (2018)
24. Crane, K.: Keenan's 3D Model Repository. (<https://www.cs.cmu.edu/~kmc Crane/Projects/ModelRepository/>)
25. Mueller, J.L., Siltanen, S.: *Linear and Nonlinear Inverse Problems with Practical Applications*. Volume 10. Siam (2012)
26. Community, B.O.: *Blender - a 3D Modelling and Rendering Package*, Stichting Blender Foundation, Amsterdam (2018)
27. Andersen, A.H., Kak, A.C.: Simultaneous Algebraic Reconstruction Technique (SART): A superior implementation of the ART algorithm. *Ultrasonic Imaging* **6** (1984)
28. Chambolle, A., Pock, T.: A First-Order Primal-Dual Algorithm for Convex Problems with Applications to Imaging. *Journal of Mathematical Imaging and Vision* **40** (2011)
29. Sidky, E.Y., Jørgensen, J.H., Pan, X.: Convex optimization problem prototyping for image reconstruction in computed tomography with the Chambolle–Pock algorithm. *Physics in Medicine and Biology* **57** (2012)
30. Roelandts, T., Batenburg, K.J., den Dekker, A.J., Sijbers, J.: The reconstructed residual error: A novel segmentation evaluation measure for reconstructed images in tomography. *Computer Vision and Image Understanding* **126** (2014)

31. Paszke, A., Gross, S., Massa, F., Lerer, A., Bradbury, J., Chanan, G., Killeen, T., Lin, Z., Gimelshein, N., Antiga, L., Desmaison, A., Köpf, A., Yang, E., DeVito, Z., Raison, M., Tejani, A., Chilamkurthy, S., Steiner, B., Fang, L., Bai, J., Chintala, S.: PyTorch: An imperative style, high-performance deep learning library. In: Neural Information Processing Systems. (2019)
32. Kingma, D., Ba, J.: Adam: A method for stochastic optimization. International Conference on Learning Representations (2015)
33. Huang, J., Su, H., Guibas, L.: Robust Watertight Manifold Surface Generation Method for ShapeNet Models. arXiv:1802.01698 [cs] (2018)
34. Attene, M.: A lightweight approach to repairing digitized polygon meshes. The Visual Computer **26** (2010)
35. Skorikov, A., Albrecht, W., Bladt, E., Xie, X., van der Hoeven, J.E.S., van Blaaderen, A., Van Aert, S., Bals, S.: Quantitative 3D Characterization of Elemental Diffusion Dynamics in Individual Ag@Au Nanoparticles with Different Shapes. ACS Nano **13** (2019)
36. Zanaga, D., Altantzis, T., Sanctorem, J., Freitag, B., Bals, S.: An alternative approach for ζ -factor measurement using pure element nanoparticles. Ultramicroscopy **164** (2016)
37. Lauterbach, C., Garland, M., Sengupta, S., Luebke, D.P., Manocha, D.: Fast BVH Construction on GPUs. Computer Graphics Forum **28** (2009)